

# $Q$ Control of an Active AFM Cantilever With Differential Sensing Configuration

M. Bulut Coskun<sup>ID</sup>, Hamed Alemansour, Anthony G. Fowler<sup>ID</sup>, *Member, IEEE*,  
 Mohammad Maroufi<sup>ID</sup>, *Member, IEEE*, and S. O. Reza Moheimani<sup>ID</sup>, *Fellow, IEEE*

**Abstract**—Microcantilevers featuring separate built-in actuation and displacement sensing capabilities allow effective and simple implementation of control methods, opening a pathway to achieving higher scan speeds in tapping-mode atomic force microscopy. Such active cantilevers are a significant milestone to eventually obtain video-rate on-chip atomic force microscopes (AFMs) that can even surpass the functionality and imaging speed of their macroscale counterparts at a significantly lower cost. In this brief, we present an active AFM cantilever with an on-chip actuator and two built-in displacement sensors, designed to be integrated into on-chip AFMs. The common feedthrough problem present in this type of architecture is addressed by a differential sensing configuration, and the revealed dynamics are used for the system identification. A positive position feedback controller is designed to actively tailor the  $Q$  factor of the cantilever. The imaging performance of the microcantilever with and without  $Q$  control is compared by attenuating the cantilever's  $Q$  factor from 177 to 15 using the feedback loop. A common artifact in high-speed scans, the parachuting effect, is mitigated, rendering higher imaging speeds achievable.

**Index Terms**—Atomic force microscopy, feedthrough cancellation (FTC), imaging, piezoelectric microcantilevers,  $Q$  control.

## I. INTRODUCTION

THE atomic force microscope (AFM) has been demonstrated to be an invaluable imaging tool in many applications [1]–[4], thanks to its subnanometer resolution with the ability to operate in various environments. In essence, the AFM collects information by scanning a sample with a compliant microcantilever featuring a sharp tip, which interacts with the surface. Depending on the operation mode, the tip and the sample surface can be in contact, intermittent contact, or noncontact conditions. Among these, intermittent contact, also known as tapping mode, has been widely preferred over the others, particularly while delicate samples in a nonvacuum environment are being scanned [5], [6].

Manuscript received March 27, 2018; accepted June 8, 2018. Manuscript received in final form June 20, 2018. This work was supported by The University of Texas at Dallas. Recommended by Associate Editor J. Li. (M. Bulut Coskun and Hamed Alemansour contributed equally to this work.) (Corresponding author: S. O. Reza Moheimani.)

M. B. Coskun, H. Alemansour, M. Maroufi, and S. O. R. Moheimani are with the Department of Mechanical Engineering, The University of Texas at Dallas, Richardson, TX 75080 USA (e-mail: bulut.coskun@utdallas.edu; hamed.alemansour@utdallas.edu; mohammad.maroufi@utdallas.edu; reza.moheimani@utdallas.edu).

A. G. Fowler was with The University of Texas at Dallas, Richardson, TX 75080 USA. He is now with Manufacturing, Materials and Mechatronics Engineering, RMIT University, Melbourne, VIC 3000, Australia (e-mail: anthony.fowler@rmit.edu.au).

Color versions of one or more of the figures in this paper are available online at <http://ieeexplore.ieee.org>.

Digital Object Identifier 10.1109/TCST.2018.2850338

During conventional tapping-mode operation, the microcantilever is excited close to its resonant frequency by using a base shaker, and the cantilever tip periodically strikes the sample surface with a set oscillation amplitude. The oscillation of the tip is tracked by means of reflecting a laser off the back of the cantilever onto a photodiode. The signal produced by the photodiode is then demodulated to determine the amplitude of oscillation of the cantilever. The cantilever is scanned over the surface by an XYZ scanner. Encountering a topographic change during the scan leads to a shift in the cantilever's resonant frequency, which consequently alters its oscillation amplitude. The difference between the set and actual oscillation amplitudes, known as the error signal, is then fed back to the Z-axis controller, where Z refers to the out-of-plane direction. The controller output drives the XYZ scanner in the Z-direction up or down to maintain the set oscillation amplitude. Here, the output of the controller is proportional to the sample height, and the topographic image can be constructed using the controller output along with the X and Y position data.

Despite its widespread use, the imaging speed in tapping-mode AFMs is limited by the transient response of the cantilever. The ability of the cantilever to effectively respond to the rate of topography change can be described in terms of its bandwidth, which is proportional to the cantilever's resonant frequency and inversely proportional to its quality factor,  $Q$  [7]–[9]. The relatively high  $Q$  of standard tapping-mode cantilevers results in a slow transient response, limiting the stability margins of the Z-axis feedback loop. Importantly, slow transients can also lead to probe loss as the cantilever encounters a sharp drop in the topography. This introduces a ramp-shaped artifact in the resulting image also known as the parachuting effect [10]. Overall, reducing the  $Q$  factor is desirable from the imaging speed perspective; however, it also results in a decline in the force sensitivity [11]. This tradeoff has been a driving force for research in active control of the  $Q$  factor of AFM cantilevers [9], [12], [13].

Commonly, the  $Q$  factor of a cantilever is modified by adding a tip velocity feedback with a gain to the actuation signal. Using this principle, many controllers have been designed in the literature, such as time delay [14]–[16], simple differentiator [8], [17], [18], resonant [9], [19], [20], and positive position feedback (PPF) [13], [21] controllers. These controllers can be employed in the standard tapping-mode AFM configuration using the base shaker excitation and laser/photodetector-based displacement sensing. However, base shaker excitation can introduce complex dynamics and distortions in the frequency response, which leads to inaccuracies

in the system identification [22]. This fact makes the use of active cantilevers with built-in actuation more preferable in control applications [13], [18].

In addition to the on-chip actuation, integrated displacement sensing, which removes the need for the bulky laser and photodiode, also has become one of the main trends in microcantilever research today [23]–[29]. Apart from the distinct merits of having on-chip sensing and actuation for conventional AFMs, these features can also be incorporated in emerging on-chip AFMs to reduce their complexity. Ruppert *et al.* [30] reported combined sensing and actuation transduction mechanisms in the microcantilever of an on-chip AFM. There, a single piezoelectric transducer was used to simultaneously actuate the microcantilever and measure the displacement to achieve tapping-mode imaging. However, this architecture came at the cost of more complex electronics and feedthrough cancellation (FTC) techniques. Coskun *et al.* [31] addressed the problems arising from the self-sensing by presenting an active cantilever featuring a separate integrated piezoelectric actuator and two sensors. There, a straightforward on-chip FTC method was proposed, enabling the actuation feedthrough signal to be reduced over a large bandwidth. This brief builds on our previous study reported in [31]. Here, the same type of microfabricated cantilever featuring on-chip actuation and differential sensing scheme with improved FTC and signal-to-noise ratio (SNR) is employed for high-speed tapping-mode imaging. The cantilever and the readout circuit are now integrated and implemented on the same printed circuit board (PCB) which not only made the FTC more robust to environmental changes but also significantly reduces the noise. Correspondingly, the SNR of the on-chip sensors is remarkably improved and is comparable to that of the conventional photodiode sensor. Furthermore, the undamped and high  $Q$  factor nature of the cantilever, which limits the achievable imaging speed and causes imaging artifacts, is addressed. A PPF controller is designed to tailor the  $Q$  factor of the cantilever on-demand and improve its bandwidth. A common imaging artifact in high-speed scans, the parachuting effect, is substantially mitigated.

## II. BACKGROUND

### A. Imaging Artifacts at Higher Scan Speeds: Parachuting

Probe loss occurs when the rate of the topography drop is faster than the rate of the cantilever's amplitude increase. During probe loss, the oscillation amplitude is no longer bounded by the surface, and the amplitude exponentially increases according to the following equation [8]:

$$A(t) = A_{\text{set}} + (A_0 - A_{\text{set}}) \left(1 - e^{-\frac{\omega_n}{2Q}t}\right) \quad (1)$$

where  $A_{\text{set}}$ ,  $\omega_n$ , and  $t$  are the set oscillation amplitude, resonant frequency of the cantilever, and time, respectively. When probe loss occurs, the oscillation amplitude saturates at the free air amplitude,  $A_0$ , until the probe lands back on the surface again. As a result, a sharp step-down in the topography would appear as a ramp in the obtained images, which is called the parachuting effect.

According to (1), the time constant is proportional to the cantilever's quality factor. Reducing the  $Q$  factor of the cantilever decreases the time constant, and consequently the oscillation amplitude reaches the free air amplitude sooner. This initially induces a larger rate of error change, which ultimately enhances the response of the Z-axis feedback controller and the actuator reestablishes the contact with the sample at a faster rate compared to the native cantilever.

### B. $Q$ Control

The  $Q$  factor of a cantilever can be modified on demand by adding the tip velocity feedback with a gain ( $G$ ), obtained by the derivative of the time-domain displacement ( $z$ ) signal to the actuation signal. This can be represented with the use of the dynamic model of the cantilever as follows [9]:

$$m\ddot{z} + \frac{m\omega_n}{Q}\dot{z} + kz = F_{\text{act}} + F_{\text{TS}} - G\dot{z} \quad (2)$$

where  $m$  is the effective mass and  $k$  is the stiffness of the cantilever. On the right-hand side, the actuation and tip-sample interaction forces are designated by  $F_{\text{act}}$  and  $F_{\text{TS}}$ , respectively. By rearranging the velocity terms in (2), the effective quality factor ( $Q^*$ ) of the cantilever can be defined by

$$\frac{m\omega_n}{Q^*} = \frac{m\omega_n}{Q} + G. \quad (3)$$

Hence, the closed-loop quality factor can be decreased by setting a positive value for the gain ( $G$ ), and vice versa.

## III. DESIGN, MICROFABRICATION, AND CIRCUITRY

### A. Piezoelectric Microcantilever Design and Fabrication

Our active cantilever has a double-sectioned geometry, comprising a large rectangular section ( $390 \mu\text{m} \times 280 \mu\text{m} \times 5 \mu\text{m}$ ), where the piezoelectric elements are located, as well as a smaller section ( $130 \mu\text{m} \times 75 \mu\text{m} \times 5 \mu\text{m}$ ) with a probe tip. There are three parallel piezoelectric elements extending over the top and along the length of the larger rectangular section. The piezoelectric layer in the middle is utilized for actuation, whereas the two located on the sides function as displacement sensors.

For the microfabrication, a silicon-on-insulator (SOI) substrate with a  $5\text{-}\mu\text{m}$ -thick Si device layer,  $2\text{-}\mu\text{m}$ -thick buried oxide (BOX), and  $450\text{-}\mu\text{m}$ -thick Si handle layer is used. First, a  $300\text{-nm}$ -thick  $\text{SiO}_2$  layer is grown on both sides of the SOI wafer via wet thermal oxidation at  $1000^\circ\text{C}$  for 35 min. This serves as an insulation layer for the upcoming metal electrodes. This is followed by the lithography, e-beam evaporation ( $15\text{-nm}/150\text{-nm}$ -thick Ti/Pt), and lift-off steps for the bottom electrode features located on top of the insulating oxide layer, respectively [see Fig. 1(a)]. Next, a  $1\text{-}\mu\text{m}$ -thick layer of AlN is sputtered, and a  $300\text{-nm}$ -thick layer of  $\text{SiO}_2$  is deposited via plasma-enhanced chemical vapor deposition. This oxide layer is then patterned and dry etched to obtain the etch mask for the AlN features. AlN etching comprises a  $\text{Cl}_2$ -based dry etching step and a quick wet etching inside a 2.5% tetramethylammonium hydroxide solution at  $80^\circ\text{C}$  to ensure the removal of the AlN from the unmasked areas [see Fig. 1(b)]. Later, the oxide mask is removed by reactive

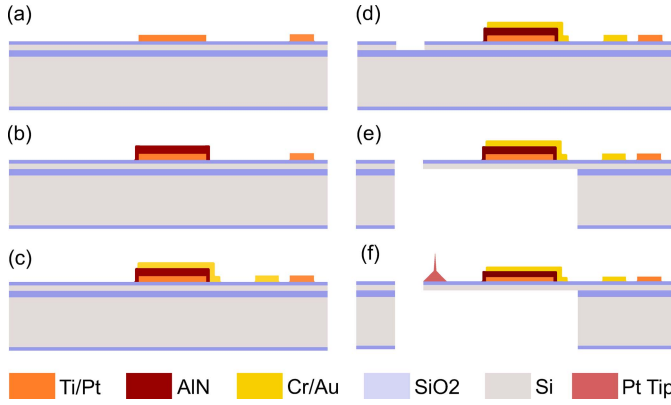


Fig. 1. Microfabrication steps. (a) Bottom electrodes (Ti/Pt) are deposited by the E-beam evaporation and lifted off. (b) Piezoelectric layer (AlN) is sputtered and etched. (c) Top electrodes (Cr/Au) are deposited by the E-beam evaporation and lifted off. (d) Thermal oxide and Si device layers are etched by using RIE and DRIE, respectively. (e) Backside is etched and devices are released. (f) Sharp Pt cantilever tip is deposited using FIB.

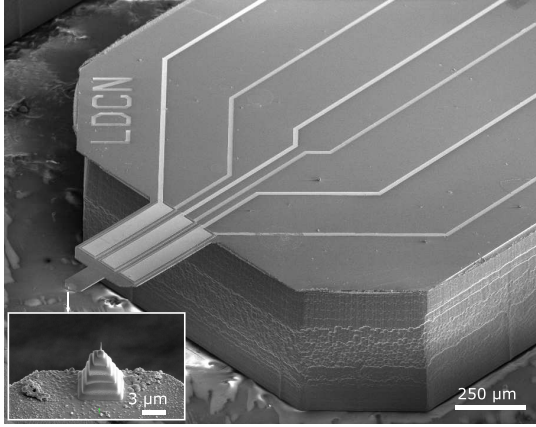


Fig. 2. SEM image of the fabricated double-sectioned cantilever. Three patches of piezoelectric layers are visible on the wider section of the cantilever.

ion etching (RIE), and the microfabrication continues with the deposition of the top electrode features through the lithography, sputtering of Cr/Au, and lift-off processes [see Fig. 1(c)]. After that, the cantilever geometry is transferred by lithography and the device layer is etched by deep RIE (DRIE) [see Fig. 1(d)]. Next, the device layer is entirely coated with a 500-nm-thick protective parylene layer prior to the backside etching, which concludes the frontside processes.

The backside processes start with the backside lithography to obtain the etch mask. Then, the oxide layer on the backside, the Si handle layer, and the BOX layer are successively etched using RIE, DRIE, and RIE processes [see Fig. 1(e)]. Lastly, the protective parylene film is removed and the device layer is cleaned by  $O_2$  plasma. An SEM image of the fabricated device is shown in Fig. 2.

For AFM imaging, a 10- $\mu$ m-high Pt tip is deposited on the fabricated cantilever by an FEI Nova Nanolab 200 focused ion beam (FIB) system. The multilevel supporting structure and the sharp tip with 30-nm radius are built by ion beam- and electron beam-assisted deposition, respectively (see Fig. 2). Finally, the devices are glued and wire bonded to a PCB for characterization.

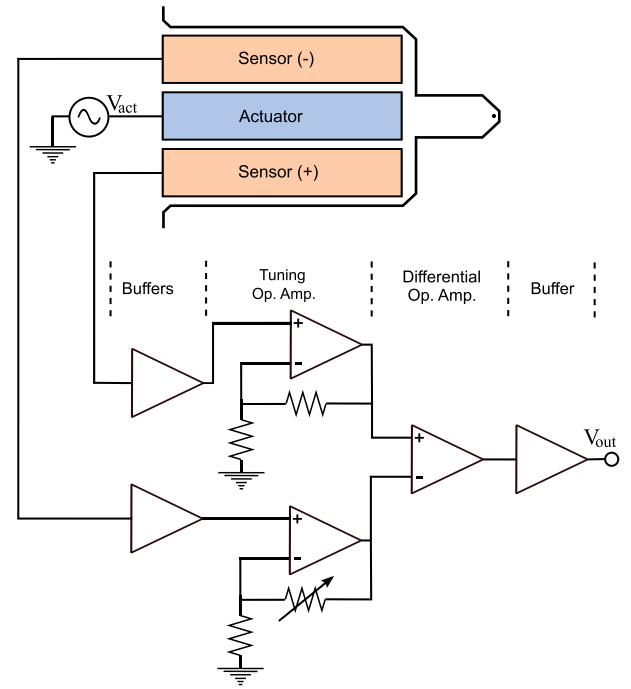


Fig. 3. Simplified schematic of the sensor readout circuit.

### B. Displacement Sensor Readout Circuit

The microcantilever features two piezoelectric layers symmetrically fabricated on the opposite sides of the actuation layer, functioning as displacement sensors. In this architecture, since the sensors and actuator are closely spaced, the sensor outputs are often perturbed by the feedthrough from the actuation signal through the parasitic capacitance. Consequently, a situation could arise that the dynamics of the cantilever at the sensor output are buried in the feedthrough, leading to a drastic decline in the obtainable dynamic range. This makes the use of microcantilevers with the integrated sensors and actuators impractical in tapping-mode AFM imaging. To address this problem, the sensors are employed in a differential configuration by reversing the polarity of one of the piezoelectric sensors. This is provided by acquiring signals from the bottom electrode of the first sensing piezoelectric transducer and the top electrode of the second piezo, while the remaining electrodes are grounded. Since the feedthrough manifests itself as a common-mode signal, the differential output obtained from the sensors contains significantly less feedthrough [31]. In order to reveal the concealed dynamics to a greater extent, a tunable gain has been added to one of the sensors' outputs to obtain a finer compensation for the additional parasitic impedances arising from the routing tracks, the bonding pads, and the readout circuit.

This method is implemented by a circuit which is built on a custom design PCB, schematically shown in Fig. 3. To minimize the effect of electrical noise on the sensor output, the circuit is implemented adjacent to the cantilever on the PCB using surface-mount device components. The first stage of the readout circuit consists of an AD8244 FET input buffer, which is used to buffer the high-impedance differential signals obtained from the piezoelectric sensors.



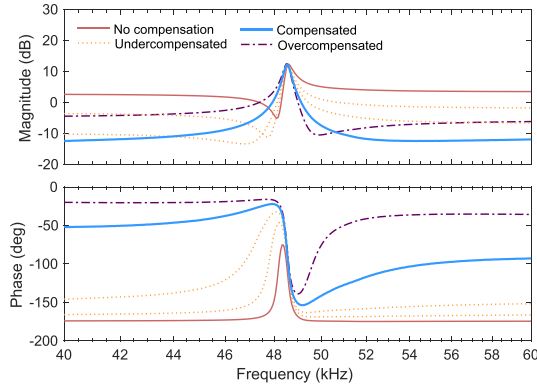


Fig. 4. Frequency response of the fabricated microcantilever from the actuation voltage to the sensor readout circuit output before and after the FTC.

This is followed by a noninverting amplifier for each of the two sensor signals. The gain of one of the amplifiers is adjustable. This enables us to tune the FTC signal as desired. These outputs are fed into an AD8421 instrumentation amplifier, which cancels the common-mode feedthrough signal and amplifies the differential cantilever displacement signal with a gain of 100 V/V. Finally, an output buffer stage is implemented using an LT6230 operational amplifier.

#### IV. OPEN-LOOP CHARACTERIZATION

##### A. Frequency Response and Feedthrough Cancellation

The frequency response from the piezoelectric actuation voltage to the differential sensor output signal conditioned by the readout circuit is measured using a Zurich Instruments HF2LI lock-in amplifier. The cantilever is driven by a swept-sine signal with 75-mV amplitude within the frequency range of 40 and 60 kHz, when the adjustment gain is set to unity. The resulting frequency response is shown in Fig. 4 (red curve), which yields a dynamic range of 8.7 dB at the resonance, indicating that the differential sensing alone mitigates the feedthrough to a certain extent. Coskun *et al.* [31] showed that the dynamic range would be an order of magnitude less if the sensors were used in a single-ended configuration. Despite the mitigated feedthrough, the superposition of the actuation voltage on the sensor output is still evident from the presence of a zero near the pole around the fundamental mode [32], and hence, the feedthrough requires further compensation.

By increasing the adjustment gain, the effect of feedthrough gradually decreases, and the frequency responses during this stage of cancellation are denoted as undercompensated in Fig. 4 (orange curve). Eventually, the feedthrough is compensated, and the dynamic range and phase at the resonance reach 23 dB and  $-90^\circ$ , respectively, as depicted in Fig. 4 (blue curve). Further increase in the gain beyond this point causes an increased mismatch between the sensors, and the feedthrough starts to become dominant again and conceal the cantilever's dynamic response, as shown in Fig. 4 (purple curve).

##### B. Signal-to-Noise Ratio

After FTC, the SNR is obtained for both the on-chip piezoelectric differential sensor and the AFM photodetector, when

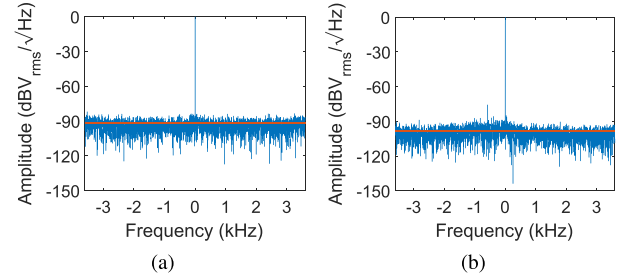


Fig. 5. SNR comparison using (a) on-chip piezoelectric sensor and (b) photodetector.

the cantilever is excited in free air at its fundamental mode with a displacement amplitude of 160 nm. For both sensing modalities, the time-domain output signals are demodulated around a bandwidth of 400 Hz, and the amplitude spectral densities are obtained by the HF2LI lock-in amplifier, as shown in Fig. 5. For comparison purposes, the measurements are normalized by shifting the peak amplitudes to 0 dB. The SNR is determined from Fig. 5(a) to be 92 and 98 dB for the piezoelectric and photodetector sensors, respectively.

##### C. System Identification

With the feedthrough canceled and the dynamics of the cantilever revealed, the open-loop transfer function of the piezoelectric cantilever from the actuation voltage to the sensor output can be identified. The truncated model of the cantilever from the piezoelectric actuation voltage to the displacement can be represented by a second-order transfer function [33], considering only the first vibrational mode. The effect of the remaining feedthrough originating from the chip body, bonding pads, and circuitry should be considered in the transfer function modeling the cantilever from the piezoelectric actuation voltage input to the piezoelectric sensor voltage output. Using the least squares method within the frequency range of 40 to 60 kHz, a bi-proper third-order transfer function is fit to the feedthrough-compensated frequency response to model the first resonance of the cantilever as

$$G(s) = \frac{-0.73s^3 + 1.28 \times 10^5 s^2 - 6.57 \times 10^{10} s + 1.45 \times 10^{16}}{s^3 + 1.12 \times 10^6 s^2 + 9.52 \times 10^{10} s + 1.05 \times 10^{17}}. \quad (4)$$

The model in (4) is then used to design a feedback controller as described in Section V.

#### V. CLOSED-LOOP CONTROLLER DESIGN AND CHARACTERIZATION

A PPF controller can be used to attenuate the first resonance of the cantilever to achieve a desired quality factor. A PPF controller is chosen for this application due to its low-pass behavior. The magnitude response of this controller decreases with a slope of  $-40$  dB/decade at high frequencies, preventing spillover of the neglected higher modes while simultaneously reducing the high frequency noise effects. By using a PPF controller in positive feedback with a negative imaginary cantilever, the robustness of the controller can be guaranteed

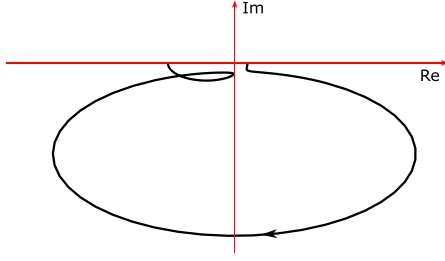
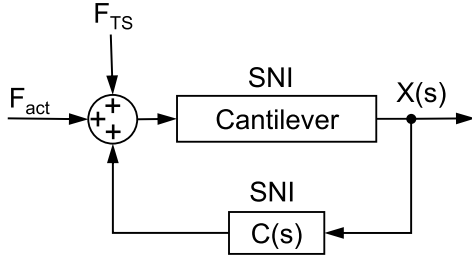


Fig. 6. Nyquist plot of cantilever's identified model.

Fig. 7. Block diagram of  $Q$  control feedback loop.  $X(s)$  is the sensor output and  $C(s)$  is the PPF controller, which represents a differentiator with a negative gain of one at the resonance frequency of the cantilever.

in the presence of uncertainties in the modal frequencies and unmodeled cantilever dynamics [34].

#### A. PPF Controller: Stability

The closed-loop stability of two systems connected by a positive feedback can be proved based on the negative-imaginary (NI) theory [34]. A single-input single-output system is a NI if all of its poles lie in the open left-half-plane (OLHP) and the phase of its frequency response is within the closed interval of  $-180^\circ$  and  $0^\circ$  for all frequencies greater than and equal to 0. If the latter condition changes to be open interval for the positive frequencies, then the system becomes strictly NI (SNI). The positive feedback interconnection of a NI transfer function,  $H(s)$ , and a SNI transfer function,  $P(s)$ , is internally stable if and only if the dc loop gain is strictly less than 1, provided that  $H(\infty)P(\infty) = 0$  and  $P(\infty) \geq 0$  [34].

The transfer function of a PPF controller can be represented as [21], [34]

$$C(s) = \frac{k_c \omega_c^2}{s^2 + 2\zeta_c \omega_c s + \omega_c^2} \quad (5)$$

where  $k_c$ ,  $\omega_c$ , and  $\zeta_c$  are positive. Since all poles of a PPF controller are in the OLHP and the phase response is within the range of  $(-\pi, 0)$  for all  $\omega > 0$ , the controller is SNI. On the other hand, the positive-frequency Nyquist plot of the identified cantilever model, reported in (4), is also plotted in Fig. 6. The plot lies below the real axis for all  $\omega > 0$ , showing that the identified model is also SNI. Hence, according to the NI theory, the closed-loop system shown in Fig. 7 is internally stable, provided that  $G(0)C(0) < 1$ . Therefore, knowing the dc gain of the system to be 0.14

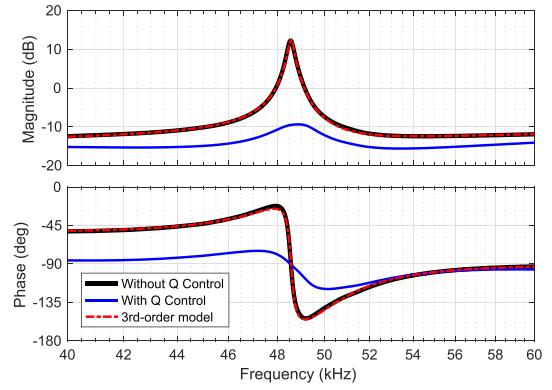
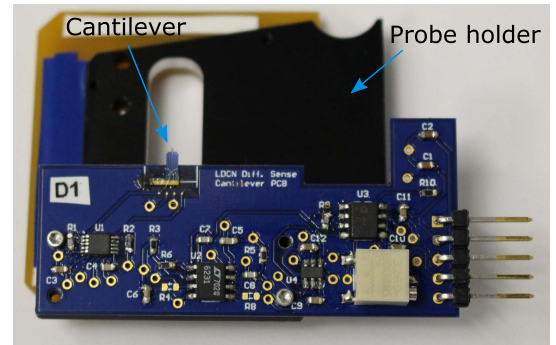
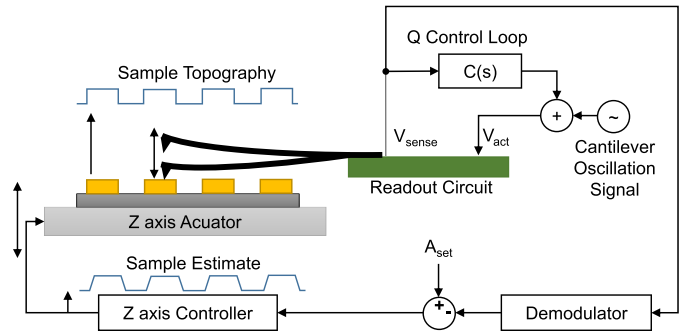
Fig. 8. Frequency response of the cantilever without and with  $Q$  control, obtained when the damping loop is open or closed, respectively. The PPF controller is used to reduce the quality factor of cantilever from 177 to 15.

Fig. 9. Photograph of the cantilever holder assembly.

Fig. 10. Block diagram of Z-axis feedback loop. The cantilever is driven at its first resonance frequency. Changes in the sample topography cause variation of the oscillation amplitude of the cantilever. The demodulated amplitude is compared with the set point amplitude, and the error signal is fed through the Z-axis controller. The sample topography is represented by the output of Z-axis controller, which by sending signal to the Z-axis actuator compensates for variations in the oscillation amplitude of cantilever due to the changes in the sample height.  $Q$  control feedback loop is also included in the block diagram.

from (4), the maximum allowable gain of the PPF controller,  $k_c$ , is 7.19. For all frequencies greater than 0, the open-loop phase response,  $\angle G(j\omega)C(j\omega)$ , is in the interval  $(-2\pi, 0)$ , which does not include the positive real axis. As a result, the Nyquist plot intersects the positive real axis only at the zero frequency. Hence, by using a controller gain within the specified range, the critical point of  $s = 1+0j$  is not encircled.

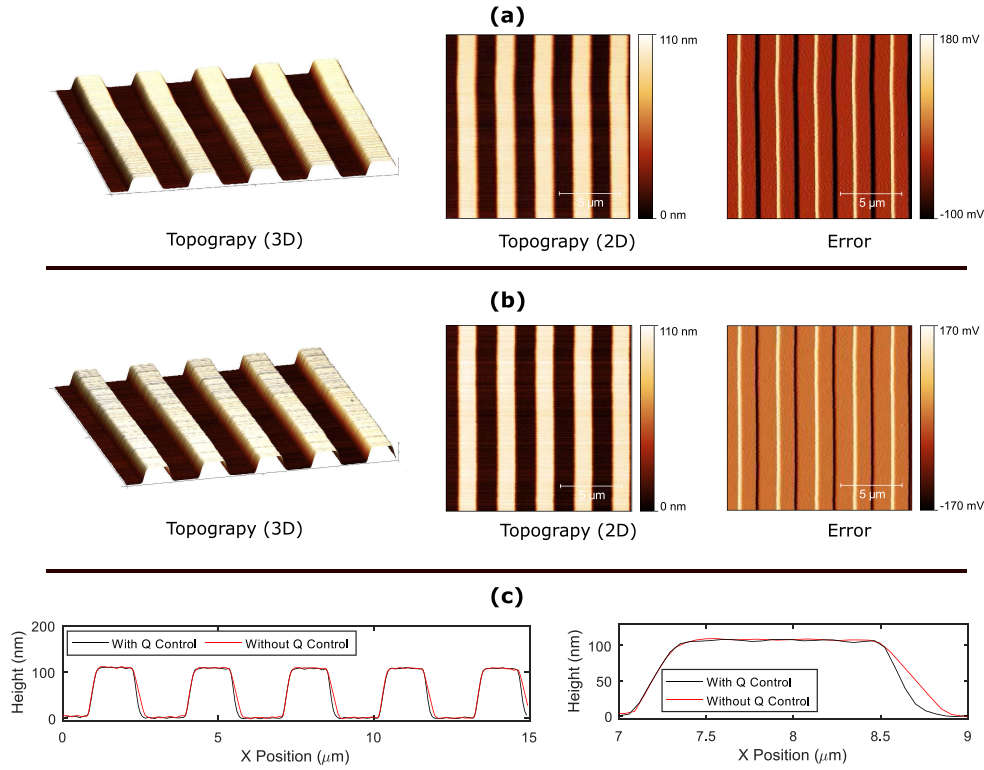


Fig. 11. AFM Images of calibration grating (a) without and (b) with  $Q$  control obtained at scanning speed of  $60 \mu\text{m/s}$ . Same controller gain was used for the both cases. Reducing the quality factor of cantilever improves its transient response. Step height of features is  $110 \pm 2 \text{ nm}$  and period is  $3.00 \pm 0.05 \mu\text{m}$ . (c) Line profiles.

### B. PPF Controller: Design and Implementation

A block diagram of the feedback controller loop to alter the quality factor of the cantilever is shown in Fig. 7. As mentioned in Section I, the effective quality factor ( $Q^*$ ) of the cantilever stated in (3) can be modified using the cantilever's tip velocity feedback. The on-chip piezoelectric sensor measures the displacement of the cantilever in the Z-direction; therefore, the velocity can be estimated from this signal. Using the displacement of the cantilever at the resonance, its velocity can be estimated by the PPF controller provided that  $\omega_c$  in (5) is chosen to be equal to the cantilever's resonance frequency. In this way, the phase delay of the PPF controller at the resonance frequency of the cantilever is equal to  $90^\circ$  and the PPF controller represents a differentiator with a negative gain [i.e.  $-\dot{z}$  in (2)]. Hence, the effective quality factor is decreased, provided that the gain of the PPF controller is positive.

The quality factor of the cantilever can be adjusted to a desired value by tuning the PPF controller parameters. There are two parameters,  $(k_c, \zeta_c)$ , that can be independently changed to achieve a desired closed-loop performance. By varying these two parameters, the position of the closed-loop poles is changed and the desired closed-loop response can be obtained. The following cost function is defined and the Nelder-Mead simplex algorithm is used in MATLAB to find the values of  $(k_c, \zeta_c)$  for which the cost function is minimum:

$$J(k_c, \zeta_c) = (Q - Q_{\text{des}})^2. \quad (6)$$

The quality factor is measured from the frequency response data using the following definition:

$$Q = \frac{f_r}{\Delta f_{-3 \text{ dB}}} \quad (7)$$

where  $f_r$  is the resonant frequency and  $\Delta f_{-3 \text{ dB}}$  is the half-power bandwidth. Using the frequency response data illustrated in Fig. 8, the open-loop quality factor of the cantilever is measured as  $Q = 177$  at the resonance frequency of  $\omega_n = 48.547 \text{ kHz}$ . The desired quality factor is set to  $Q_{\text{des}} = 15$ . Using the cost function (6), controller parameters  $k_c$  and  $\zeta_c$  are obtained as 0.959 and 0.178, respectively.

The controller is implemented using an Anadigm QuadApex AN231E04 field-programmable analog array (FPAA), and the frequency response of the system is recorded and compared with the open-loop response in Fig. 8. The recording is performed using an HF2LI lock-in amplifier in the frequency range from 40 to 60 kHz. As is visible, the cantilever is significantly damped, while its  $Q$  factor is reduced from 177 to the set value of 15.

## VI. IMAGING PERFORMANCE

### A. Experimental Setup

The piezoelectric cantilever is mounted on and wire bonded to the readout PCB, which is then attached to the probe holder via a custom designed 3-D printed adapter, as illustrated in Fig. 9. The PCB with the holder is then inserted into a commercially available AFM (AFMWorkshop TT-AFM) for imaging tests.

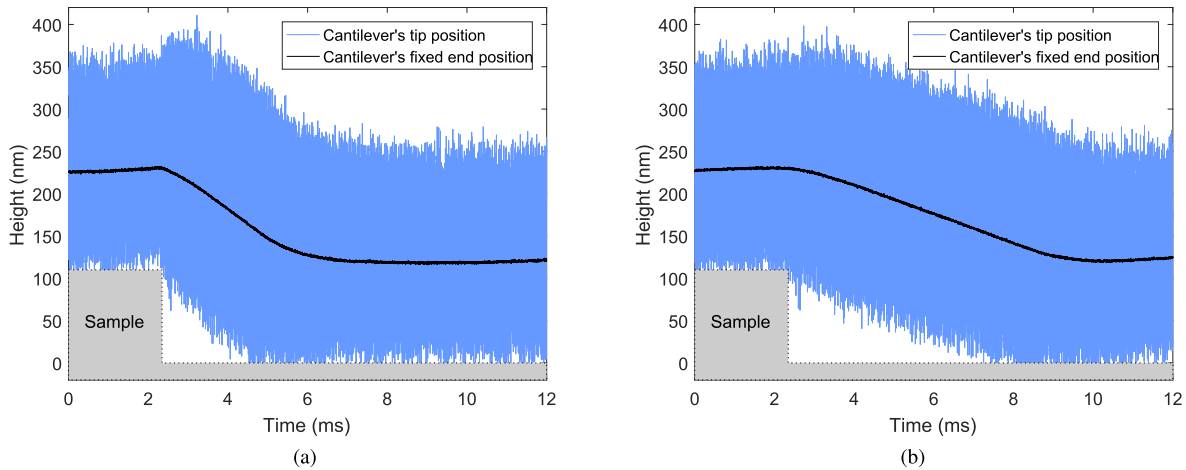


Fig. 12. Cantilever's fixed end and the tip position as it scans over a sharp downward step (a) with and (b) without  $Q$  control.

The laser/photodetector of the AFM and the base shaker are electronically bypassed during the test, whereas the on-chip differential sensor signal is injected to the AFM's electronic board, providing the displacement signal. An external signal source is used for the excitation of the cantilever. Also, as mentioned in the previous section,  $Q$  control is implemented externally using the FPAA. Other than these, the embedded components of the commercial AFM, including XY scanner, Z actuator, Z-axis controller, and demodulator, are utilized for the scan. The X and Y positions and the corresponding Z-axis controller outputs are obtained by the AFM's software to construct images (see Fig. 10). In addition, the sensor output, the demodulated amplitude, and the Z-axis drive output are also separately recorded in the time domain using a data acquisition system (Spectrum Digitizer NETBOX) with a sampling frequency of 1 MHz for further analysis.

### B. Imaging

To demonstrate the effect of  $Q$  control on the transient response of the cantilever, AFM images of an NT-MDT TGZ2 calibration grating featuring  $110 \pm 2$  nm high rectangular steps with a period of  $3.00 \pm 0.05$   $\mu\text{m}$  are obtained. The scan area and the line speed were set to  $15 \mu\text{m} \times 15 \mu\text{m}$  and 60  $\mu\text{m/s}$ , respectively. Images were obtained with and without the  $Q$  control for comparison, and 3-D and 2-D topography and error images are shown in Fig. 11(a) and (b). It can be observed that the 2-D topography image obtained with the damped cantilever is sharper compared with the open-loop case. The contrast between the two images becomes more pronounced on the edges, where the topography sharply drops. This is also visible in the error images highlighting saturation at the edges without  $Q$  control, leading to a deviation from the true topography. Hence, with no  $Q$  control, a sharp step-down in the topography appears as a ramp, as shown by the line profiles in Fig. 11(c).

To clearly see the effect of  $Q$  control on the cantilever's transient response, the recorded time-domain signals with and without  $Q$  control are plotted in Fig. 12. The free air oscillation amplitude and the set-point amplitude are adjusted

approximately to 160 and 120 nm, respectively. A constant calibration factor obtained from an MSA-100-3-D laser doppler vibrometer is used to convert the sensor voltage to the cantilever's tip displacement relative to its fixed end. The fixed-end displacement of the cantilever relative to the sample is shown in Fig. 12 (black curve) using the Z-drive voltage signal, which is calibrated assuming the 110-nm feature heights for the sample. Using these two sets of data, the cantilever's tip position relative to the sample is plotted with and without  $Q$  control in Fig. 12(a) and (b), respectively. Reducing the  $Q$  factor of the cantilever significantly helps to lower the effect of parachuting, when the tip scans over a sharp downward step in the sample.

## VII. CONCLUSION

The relatively high  $Q$  factor of AFM cantilevers in air is one of the major limitations to achieve faster scan speeds in tapping-mode AFM, as it results in a slower transient response of the cantilever. Being able to actively control the  $Q$  factor of a cantilever, featuring separate on chip sensors and actuators is a significant milestone to obtain high-speed on-chip AFM. Here, we have demonstrated the implementation of  $Q$  control on our custom-designed active microcantilever. The feedthrough has been canceled through a simple on-chip method by using a differential sensing method. Importantly, integrating the cantilever with the readout circuit on the same PCB has not only made the FTC more robust but also has drastically improved the SNR of the displacement sensors. Following the recovery of the dynamics, the system was identified and a PPF controller was implemented that was capable of reducing the  $Q$  factor of the cantilever by a factor of 11 with guaranteed stability. The effect of  $Q$  control on the cantilever's transient response has been illustrated via fast AFM imaging. Future work will focus on integrating the current cantilever, FTC, and  $Q$  control concepts with a new generation on-chip AFM to further increase the scan speeds.

## ACKNOWLEDGMENT

The authors would like to thank The University of Texas at Dallas Cleanroom Research Laboratory for the facilities



provided which were used to fabricate the cantilevers demonstrated in this brief.

## REFERENCES

- [1] Y. H. Guu, "AFM surface imaging of AISI D2 tool steel machined by the EDM process," *Appl. Surf. Sci.*, vol. 242, no. 3, pp. 245–250, 2005.
- [2] M. Göken and M. Kempf, "Microstructural properties of superalloys investigated by nanoindentations in an atomic force microscope," *Acta Mater.*, vol. 47, no. 3, pp. 1043–1052, 1999.
- [3] S. Krämer, R. R. Furer, and C. B. Gorman, "Scanning probe lithography using self-assembled monolayers," *Chem. Rev.*, vol. 103, no. 11, pp. 4367–4418, 2003.
- [4] T. Watanabe-Nakayama, K. Ono, M. Itami, R. Takahashi, D. B. Teplow, and M. Yamada, "High-speed atomic force microscopy reveals structural dynamics of amyloid  $\beta$ 1–42 aggregates," *Proc. Nat. Acad. Sci. USA*, vol. 113, no. 21, pp. 5835–5840, 2016.
- [5] R. Höper, T. Gesang, W. Possart, O.-D. Hennemann, and S. Boseck, "Imaging elastic sample properties with an atomic force microscope operating in the tapping mode," *Ultramicroscopy*, vol. 60, no. 1, pp. 17–24, 1995.
- [6] P. Schön, "Imaging and force probing RNA by atomic force microscopy," *Methods*, vol. 103, pp. 25–33, Jul. 2016.
- [7] J. D. Adams, B. W. Erickson, J. Grossenbacher, J. Brugger, A. Nievergelt, and G. E. Fantner, "Harnessing the damping properties of materials for high-speed atomic force microscopy," *Nature Nanotechnol.*, vol. 11, no. 2, pp. 147–151, Nov. 2016.
- [8] T. Sulchek, G. G. Yaralioglu, C. F. Quate, and S. C. Minne, "Characterization and optimization of scan speed for tapping-mode atomic force microscopy," *Rev. Sci. Instrum.*, vol. 73, no. 8, pp. 2928–2936, 2002.
- [9] M. Fairbairn and S. O. R. Moheimani, "Resonant control of an atomic force microscope micro-cantilever for active  $Q$  control," *Rev. Sci. Instrum.*, vol. 83, no. 8, p. 083708, 2012.
- [10] N. Kodera, M. Sakashita, and T. Ando, "Dynamic proportional-integral-differential controller for high-speed atomic force microscopy," *Rev. Sci. Instrum.*, vol. 77, no. 8, p. 083704, 2006.
- [11] T. R. Albrecht, P. Grütter, D. Horne, and D. Rugar, "Frequency modulation detection using high- $Q$  cantilevers for enhanced force microscope sensitivity," *J. Appl. Phys.*, vol. 69, no. 2, pp. 668–673, 1991.
- [12] M. W. Fairbairn and S. O. R. Moheimani, "Control techniques for increasing the scan speed and minimizing image artifacts in tapping-mode atomic force microscopy: Toward video-rate nanoscale imaging," *IEEE Control Syst.*, vol. 33, no. 6, pp. 46–67, Dec. 2013.
- [13] M. G. Ruppert and S. O. R. Moheimani, "Multimode  $Q$  control in tapping-mode AFM: Enabling imaging on higher flexural eigenmodes," *IEEE Trans. Control Syst. Technol.*, vol. 24, no. 4, pp. 1149–1159, Jul. 2016.
- [14] J. Tamayo, A. D. L. Humphris, R. J. Owen, and M. J. Miles, "High- $Q$  dynamic force microscopy in liquid and its application to living cells," *Biophys. J.*, vol. 81, no. 1, pp. 526–537, 2001.
- [15] A. D. L. Humphris, A. N. Round, and M. J. Miles, "Enhanced imaging of DNA via active quality factor control," *Surf. Sci.*, vol. 491, no. 3, pp. 468–472, 2001.
- [16] L. Chen, X. Yu, and D. Wang, "Cantilever dynamics and quality factor control in AC mode AFM height measurements," *Ultramicroscopy*, vol. 107, nos. 4–5, pp. 275–280, 2007.
- [17] J. Mertz, O. Marti, and J. Mlynek, "Regulation of a microcantilever response by force feedback," *Appl. Phys. Lett.*, vol. 62, no. 19, pp. 2344–2346, 1993.
- [18] T. Sulchek *et al.*, "High-speed tapping mode imaging with active  $Q$  control for atomic force microscopy," *Appl. Phys. Lett.*, vol. 76, no. 11, pp. 1473–1475, 2000.
- [19] D. Halim and S. O. R. Moheimani, "Spatial resonant control of flexible structures-application to a piezoelectric laminate beam," *IEEE Trans. Control Syst. Technol.*, vol. 9, no. 1, pp. 37–53, Jan. 2001.
- [20] S. O. R. Moheimani and B. J. G. Vautier, "Resonant control of structural vibration using charge-driven piezoelectric actuators," *IEEE Trans. Control Syst. Technol.*, vol. 13, no. 6, pp. 1021–1035, Nov. 2005.
- [21] M. W. Fairbairn, P. Müller, and S. O. R. Moheimani, "Sensorless implementation of a PPF controller for active  $Q$  control of an AFM microcantilever," *IEEE Trans. Control Syst. Technol.*, vol. 22, no. 6, pp. 2118–2126, Nov. 2014.
- [22] M. G. Ruppert and S. O. R. Moheimani, "High-bandwidth multimode self-sensing in bimodal atomic force microscopy," *Beilstein J. Nanotechnol.*, vol. 7, no. 1, pp. 284–295, 2016.
- [23] M. Dukic, J. D. Adams, and G. E. Fantner, "Piezoresistive AFM cantilevers surpassing standard optical beam deflection in low noise topography imaging," *Sci. Rep.*, vol. 5, Nov. 2015, Art. no. 16393.
- [24] G. E. Fantner *et al.*, "Use of self-actuating and self-sensing cantilevers for imaging biological samples in fluid," *Nanotechnology*, vol. 20, no. 43, p. 434003, 2009.
- [25] M. Li, H. X. Tang, and M. L. Roukes, "Ultra-sensitive NEMS-based cantilevers for sensing, scanned probe and very high-frequency applications," *Nature Nanotechnol.*, vol. 2, no. 2, pp. 114–120, 2007.
- [26] S. C. Minne, S. R. Manalis, and C. F. Quate, "Parallel atomic force microscopy using cantilevers with integrated piezoresistive sensors and integrated piezoelectric actuators," *Appl. Phys. Lett.*, vol. 67, no. 26, pp. 3918–3920, Oct. 1995.
- [27] S. C. Minne, S. R. Manalis, A. Atalar, and C. F. Quate, "Contact imaging in the atomic force microscope using a higher order flexural mode combined with a new sensor," *Appl. Phys. Lett.*, vol. 68, no. 10, pp. 1427–1429, 1996.
- [28] S. C. Minne *et al.*, "Automated parallel high-speed atomic force microscopy," *Appl. Phys. Lett.*, vol. 72, no. 18, pp. 2340–2342, 1998.
- [29] H.-J. Nam *et al.*, "Calibration of non linear properties of  $\text{Pb}(\text{Zr}, \text{Ti})\text{O}_3$  cantilever using integrated piezoresistive sensor for high speed atomic force microscopy," *Jpn. J. Appl. Phys.*, vol. 41, no. 11S, p. 7153, 2002.
- [30] M. G. Ruppert, A. G. Fowler, M. Maroufi, and S. O. R. Moheimani, "On-chip dynamic mode atomic force microscopy: A silicon-on-insulator MEMS approach," *J. Microelectromech. Syst.*, vol. 26, no. 1, pp. 215–225, Feb. 2017.
- [31] M. B. Coskun, A. G. Fowler, M. Maroufi, and S. O. R. Moheimani, "On-chip feedthrough cancellation methods for microfabricated AFM cantilevers with integrated piezoelectric transducers," *J. Microelectromech. Syst.*, vol. 26, no. 6, pp. 1287–1297, Dec. 2017.
- [32] M. G. Ruppert and S. O. R. Moheimani, "A novel self-sensing technique for tapping-mode atomic force microscopy," *Rev. Sci. Instrum.*, vol. 84, no. 12, p. 125006, 2013.
- [33] S. O. R. Moheimani and A. J. Fleming, *Piezoelectric Transducers for Vibration Control and Damping*. London, U.K.: Springer, 2006.
- [34] I. R. Petersen and A. Lanzon, "Feedback control of negative-imaginary systems," *IEEE Control Syst.*, vol. 30, no. 5, pp. 54–72, Oct. 2010.